HHS Public Access
Author manuscript

Mechanisms of Dynamic Nuclear Polarization in Insulating Solids

T.V. Can, **Q.Z. Ni**, and **R.G. Griffin**
Francis Bitter Magnet Laboratory and Department of Chemistry, Massachusetts, Institute of Technology, Cambridge, MA 02139

Abstract

Dynamic nuclear polarization (DNP) is a technique used to enhance signal intensities in NMR experiments by transferring the high polarization of electrons to their surrounding nuclei. The past decade has witnessed a renaissance in the development of DNP, especially at high magnetic fields, and its application in several areas including biophysics, chemistry, structural biology and materials science. Recent technical and theoretical advances have expanded our understanding of established experiments: for example, the cross effect DNP in samples spinning at the magic angle. Furthermore, new experiments suggest that our understanding of the Overhauser effect and its applicability to insulating solids needs to be re-examined. In this article, we summarize important results of the past few years and provide quantum mechanical explanations underlying these results. We also discuss future directions of DNP and current limitations, including the problem of resolution in protein spectra recorded at 80–100 K.

1. Introduction

The history of dynamic nuclear polarization (DNP) dates from 1953 when Overhauser proposed that irradiation of electron paramagnetic resonance (EPR) transitions could result in the enhancement of the polarization of coupled nuclei. [1]. Shortly thereafter, Carver and Slichter performed the first DNP experiments that confirmed the Overhauser effect (OE). In particular, they observed enhanced ^{7}Li signal intensities obtained from Li metal dispersed in mineral oil [2]. The enhancement was also observed in solutions of Na^+ in liquid NH_3 [3]. The first DNP mechanism documented for insulating solids was the solid effect (SE) and was described by Jefferies [4; 5] and Abragam and coworkers [6; 7]. Five years later, the cross effect DNP mechanism was observed by Kessennikh [8; 9], and subsequently discussed in more detail by Hill and Hwang [10; 11] and Wollan [12; 13]. The goal of many of these early efforts was to understand the physics underlying DNP and to develop experiments that produced polarized targets for neutron scattering experiments. Indeed, preparation of polarized targets remains an area of active interest in experimental particle

physics, most recently using pulsed DNP methods (*vide infra*). For the interested reader there are excellent reviews of these early experiments [14–17]

In the 1980s and early 1990s, efforts to incorporate DNP into magic angle spinning (MAS) and other solid state NMR experiments were initiated by Wind [18] *et al.*, Yannoni [19–21] and Schaefer *et al.* [22]. These experiments used klystron microwave sources and were performed primarily at a magnetic field of 1.4 T (60 MHz/40 GHz ^{1}H/electron Larmor frequencies) although one experiment at 1.9 T was reported [23]. However, these experiments were limited to low fields because of the paucity of microwave sources operating above 40–50 GHz. In 1993 Becerra, et al. [24] introduced the gyrotron as a microwave source for DNP experiments at 5 T (140 GHz for electrons), with the specific aim of developing an experimental approach that would permit DNP at higher magnetic fields used for contemporary NMR experiments. These magnetic fields require microwave sources that ideally operate at the 10–100 watt level in the ~140–660 GHz frequency range, corresponding to magnetic fields of ~5–23 T and ^{1}H Larmor frequencies of ~200–1000 MHz. Subsequently, gyrotron based DNP/NMR spectrometers operating at 250 GHz/380 MHz and 460 GHz/700 MHz were successfully constructed [25–28]. In addition, DNP/NMR instruments operating at 263 GHz/400 MHz, 395 GHz/600 MHz and 527 GHz/800 MHz are now available commercially. The accessibility of this new instrumentation has stimulated a variety of new applications as well as investigations of new DNP mechanisms.

In this review, we discuss key aspects of several known DNP mechanisms including continuous wave (CW) and time domain DNP. We present recent experimental results together with some new quantum mechanical treatments. Our analysis builds on the work by Hu *et al.* [29]. However, we emphasize the use of perturbation theories (both time independent and time dependent; non-degenerate and degenerate). Furthermore, we include the effects of MAS in CE DNP that have been considered recently [30; 31]. Our discussion focuses primarily on the mechanisms of DNP in insulating solids at high fields. For other aspects of DNP such as instrumentation, radical development, applications, etc., we refer the reader to other reviews by Ni *et al.* [32], Barnes *et al.* [33], Maly *et al.* [34], and Nanni *et al.* [35]. However, we do include a discussion of the effects of low temperature on resolution in spectra of proteins.

The paper is organized as follows. In **Sections 2.1 and 2.2**, we discuss CW DNP mechanisms in which the microwave fields are treated as time-dependent harmonic perturbations, while the remaining terms in the Hamiltonian are viewed as static. Diagonalization of the static Hamiltonian is conveniently approximated using time independent perturbation theory, without obscuring any conclusions. In the case of CE DNP (**Section 2.2**), despite the magic angle spinning, the Hamiltonian can also be regarded as static at each rotor angle. **Section 3.1** deals with pulsed DNP methods using low microwave power including DNP in the nuclear rotating frame (NRF DNP) and the dressed state solid effect (DSSE) in which the microwave fields are treated as a perturbation. In **Section 3.2**, we discuss two time-domain DNP experiments: nuclear orientation via electron spin locking (NOVEL) and the integrated solid effect (ISE), where the microwave fields are large and

can no longer be treated as perturbations. **Section 4** discusses resolution in low temperature spectra and some future directions of DNP.

2. CW DNP

2.1. Narrow EPR spectrum

The first class of DNP mechanisms in insulating solids involves radical dopants that satisfy the inequality $\delta, \; < \omega_{0I}$, where δ, and ω_{0I} are the homogenous electron paramagnetic resonance (EPR) linewidth, the breadth of the EPR spectrum and the nuclear Larmor frequency, respectively. In this case, DNP is mediated by the Overhauser effect and/or the solid effect. The influence of MAS can be conveniently ignored because the EPR spectrum is narrow and therefore the electron energy levels are only weakly modulated by the sample rotation. The molecular structures of four narrow line polarizing agents are shown in Figures 1a–d and include 1,3-bisphenylene-2-phenylallyl (BDPA), sulfonated-BDPA (SA-BDPA), trityl OX063 and Gd^{3+}-DOTA. These polarizing agents have small a g-anisotropy or, in the case of Gd^{3+} a narrow $-\frac{1}{2} \rightarrow \frac{1}{2}$ central EPR transition due to molecular symmetry. However, the EPR lines are broadened by the proton hyperfine couplings (BDPA and SA-BDPA), residual g-anisotropy (trityl OX063), or second order zero field splitting (Gd^{3+}-DOTA).

2.1.1. Overhauser effect—The Overhauser effect was the first DNP mechanism proposed for systems with mobile electrons, namely conducting solids and liquids. The effect is operative in a two-spin system consisting of one electron and one nucleus (Figure 1e), and relies on the presence of the zero quantum (ZQ) and double quantum (DQ) relaxation pathways with differing relaxation rates. The imbalance between the two rates, (Γ_0 and Γ_2 in Figure 1e) leads to an enhancement in nuclear polarization. In particular, upon microwave irradiation near the single quantum (SQ) EPR transition, the DQ and ZQ relaxation, mediated by molecular tumbling in liquids and translational motion of electrons in conducting solids, redistribute the populations via fluctuations of the anisotropic and isotropic couplings, respectively. This results in a Zeeman field profile that is symmetrically centered at the frequency of the EPR transition. In liquids, the DQ transition is generally the dominant relaxation pathway, and leads to the observation of negative DNP enhancements for [1]H. However in insulating solids, we recently observed a significant OE DNP with a _positive_ enhancement, indicating that the ZQ term is dominant [36]. This is illustrated in Zeeman field profiles of Figures 1g–1i where the positive enhancement in the center of the profiles is assigned to the OE. In addition, quantum mechanical simulations predict an OE even though the samples are insulators. In contrast to some other CW DNP mechanisms, the OE relies on allowed EPR transitions, requires much less microwave power, and appears to scale favorably with the magnetic field as is also illustrated in the panels in Figure 1g–1i.

To date the OE in insulators has only been observed for BDPA and its derivative SA-BDPA. In addition, perdeuteration of BDPA resulted in an order of magnitude decrease in DNP efficiency but, more importantly, in a sign change of the OE enhancement from positive to _negative_ as well. This result suggests that [1]H-e[−] hyperfine coupling is essential for the OE and ~ 5 MHz ^{1}H couplings are present in BDPA. This also provides an explanation of why

the OE is not observed for the trityl radical. In particular, trityl was designed to eliminate all ^{1}H couplings in order to have a narrow line to enhance Overhauser effects in solution. !

Efforts are underway to improve the efficiency of the OE with the synthesis of new narrow-line radicals with hyperfine couplings larger than those found in BDPA. Furthermore, theoretical and experimental research is needed to fully understand the origin of cross relaxation mechanisms responsible for the OE in insulating solids.

2.1.2. Solid effect—The solid effect (SE) is similar to the OE in that it involves a two-spin process between an electron spin S and nuclear spin I. The Zeeman field profiles for the SE (plus the OE) are shown in Figure 1g–1i and the SE is responsible for the negative and positive signal enhancements at $\omega_{SE} = \omega_e \pm \omega_{0I}$. In the secular approximation, the static Hamiltonian for such a system can be written as

$$H = \omega_{0S} S_z - \omega_{0I} I_z + A S_z I_z + B S_z I_x \quad (2.1.1)$$

where the first two terms are the electron and nuclear Zeeman interactions, and the last two terms the secular and pseudo-secular hyperfine couplings, respectively. Using first order perturbation theory we rewrite H as

$$H = H^{(0)} + H^{(1)} \quad (2.1.2)$$

where the small perturbation $H^{(1)}$ is the pseudo-secular hyperfine coupling term in 2.1.1. The unperturbed Hamiltonian $H^{(0)}$ is already diagonal in the direct product basis set. The energy levels and the corresponding eigenstates of H can then be evaluated using perturbation theory. The direct product states are not eigenstates of H and there is a small but essential mixing of these states due to the pseudo-secular hyperfine coupling (Figure 1f). The degree to which the states are mixed is given by the factor q [37]

$$q \approx \frac{B}{2\omega_{0I}} \quad (2.1.3)$$

As a result, the nominally forbidden ZQ and DQ transitions become slightly allowed and can be driven by the microwave field, yielding an enhancement in the nuclear polarization that is positive or negative depending on the field position relative to the position of the EPR line. We refer to the plots shown in Figures 1g–1i as Zeeman field profiles. Note that in this CW DNP experiment the coefficient of state mixing is proportional to ω_0^{-1}, and therefore the transition probability is ω_0^{-2}. Thus, the SE enhancements decrease significantly at higher fields, which is a characteristic of continuous wave (CW) DNP experiments. On the other hand, the transition rate can be improved by increasing the microwave field strength [38; 39]. Another approach is to use a radical whose EPR linewidth is progressively narrowed with the magnetic field as demonstrated by Corzilius *et al.* using high spin transition metal ions [40]. An enhancement of 144 at 5 T has been reported using trityl-OX063 radical [39].

The Hamiltonian can also be expressed as a direct sum

$$H = H_{13} \oplus H_{24} \quad (2.1.4)$$

where H_{13} and H_{24} are the Hamiltonians in the electron spin up and spin down subspaces, respectively. Accordingly, diagonalization of H in each subspace is straightforward, because H_{13} and H_{24} are both *2×2* matrices. This approach was used in the work by Hu *et al.* [29].

2.2. Cross effect

A third class of DNP experiments requires that the EPR spectra of the polarizing agents be inhomogenously broadened by the *g*-anisotropy and that the spectral breadth be large compared to the nuclear Larmor frequencies. Thus, in these "cross effect" (CE) experiments the inequality $\delta < \omega_{0I} <$　is satisfied [8; 9], and it is possible to have a <u>three spin</u> polarization transfer by satisfying the matching condition $\omega_{0I} = \omega_{0S_1} - \omega_{0S_2}$. Here, the subscripts refer to the nuclear Larmor frequencies and the two electrons whose Larmor frequencies are separated by the g-value differences, respectively. To date, the most efficient CE DNP is observed with biradicals containing two tethered nitroxide moieties, where the electron-electron coupling is 20–35 MHz [41–43]. Hu *et al.* presented a quantum mechanical description of the CE DNP in static samples [29]. Recent experimental data show that the effect of MAS is essential in understanding CE DNP. For example, there is significant signal quenching in DNP experiments during MAS but not for static samples [44]. It is therefore important to take into account the effect of sample spinning.

It is worth noting that in some circumstances the CE and SE are simultaneously present, such as, in static samples at low temperatures (~10 K) doped with either the monoradical TEMPOL [45] or the biradical TOTAPOL [46], but we refer the reader to the literature for a discussion of this case. Another topic that will not be discussed in detail in this article is the thermal mixing mechanism which requires that $\delta > \omega_{0I}$, that is a homogeneously broaden EPR spectrum. Thermal mixing has been studied recently with simulations by Hovav *et al.* [47], but to date it has not been of great practical importance for high field DNP since most of the EPR spectra are inhomogeneously broadened. Thus, at higher temperatures (~80–110 K) where most MAS experiments are being performed, the CE is dominant.

2.2.1. Cross effect DNP Zeeman field profiles—In order to establish the DNP mechanism that is present and to optimize the DNP enhancement, it is customary to record the enhancement as a function of the Zeeman field as illustrated in Figure 1 above and here we show Zeeman field profiles for the CE. In Figure 2a we show the ^{1}H and ^{13}C DNP field profiles of biradical TOTAPOL, and Figure 2b compares the ^{2}H DNP Zeeman field profiles obtained with TOTAPOL and the narrow-line monoradical trityl-OX063 [48; 49]. The enhancements were normalized to the maximum positive enhancement. For TOTAPOL, the ^{1}H, ^{13}C and ^{2}H field profiles span roughly the EPR line with the maximum positive and maximum negative enhancements appearing at the high and low field sides, respectively. For ^{1}H, the maximum enhancement is at the positive field position and the asymmetry between the maximum positive and the maximum negative enhancements is ~ 20%. [13]C and ^{2}H, which are both low-γ nuclei and relatively close in Larmor frequency, show almost identical field profiles. An asymmetry of ~20% was also observed for ^{13}C and ^{2}H, but the maximum enhancement is located at the negative field position. The reason for this

difference is that the nuclear Zeeman frequencies for ^{13}C $(\omega_{0^{13}C}=53\text{MHz})$ and ^{2}H $(\omega_{0^2H}=32.4\text{MHz})$ fit into the ~ 20 G field interval (~4.9690–4.9710 T, ~56 MHz) which is the region where the largest number of electrons per Gauss occurs in the EPR spectrum. In contrast the largest ^{1}H enhancement requires a separation of 211 MHz, which in turn requires a larger spectral breadth leading the profile shown in Figure 2a.

The ^{2}H DNP field profile of trityl-OX063 suggests that cross effect is the dominating mechanism, consistent with the fact that the EPR linewidth of trityl satisfies the CE condition for ^{2}H. This is also the case for other low gamma nuclei such as ^{17}O [50]. For these nuclei, the CE using trityl is more efficient than biradicals such as TOTAPOL due to the narrow EPR linewidth, which permits a larger fraction of the electrons to participate in the DNP processes. For example, Maly *et al.* obtained a factor of ~ 4 higher in the enhancement using trityl rather than TOTAPOL [49].

Figure 2c shows the ε=400 obtained with the biradical AMUPol, the most efficient biradical currently available [43], at 380 MHz/250 GHz. Overall, AMUPol provides approximately twofold larger DNP enhancements when compared to TOTAPOL. The improvement in the DNP efficiency can be attributed to the shorter intramolecular tether between the electron pairs, which increases the e$^-$-e$^-$ dipole coupling from ~23 MHz in TOTAPOL to ~35 MHz in AMUPol. In addition, the four methyl groups on the TEMPO rings are replaced by two tetrahydropyran rings which increases the electronic relaxation times [41] [43] [51]. Finally, the water solubility of AMUPol is greatly improved by addition of the polyethylene glycol chain.

2.2.2. The Hamiltonian—Figure 3a shows that the efficiency of the CE increases with spinning frequency ($\omega_r/2\pi$) [52], necessitating a description that includes the MAS effect. This effect was observed initially by K. Hu [53] and has been explored more recently by Mentink-Vigier *et al.* Using quantum mechanical simulations [30]. Concurrently, Thurber *et al.* independently presented a study of the CE in MAS experiments using a combination of theoretical analysis and simulations [31]. Both studies highlighted the importance of the dynamical behavior near the avoided level crossings (*vide infra*). The center piece of the simulations performed by both groups is the calculation of the time evolution of the quantum mechanical system. Due to the periodicity of the Hamiltonian in an MAS experiment, the time evolution can be evaluated by repeatedly applying the time evolution operator each rotor period. Calculation of the evolution operator during one rotor period was done in a stepwise manner and the orientation of the rotor was incremented (Figure 3b–e).

Here, we present an alternative approach based on a straightforward application of perturbation theory that can be used to understand important aspects of MAS CE. We begin with the Hamiltonian of a three-spin 1/2 system consisting of two electron spins S_1, S_2 and one nuclear spin *I*. We then decompose the Hamiltonian into an unperturbed part and a small perturbation from the pseudo-secular hyperfine coupling. The unperturbed Hamiltonian is block diagonal with four *2×2* blocks which can be diagonalized with minimum effort. The unperturbed energy levels give a good approximation of the electron-microwave crossing.

The degeneracy at the central energy levels results in either electron-electron crossing or three-spin crossing. More detailed calculations are presented below.

After a secular approximation, the Hamiltonian has the form

$$H = \omega_{0S_1} S_{1z} + \omega_{0S_2} S_{2z} - \omega_{0I} I_z + (A_1 S_{1z} + A_2 S_{2z}) I_z + (B_1 S_{1z} + B_2 S_{2z}) I_x + d \left(3 S_{1z} S_{2z} - \vec{S}_1 \vec{S}_2 \right) - 2J \vec{S}_1 \vec{S}_2 \quad (2.2.1)$$

where ω_{0S_1}, ω_{0S_2} and ω_{0I} are Larmor frequencies. A_1 and A_2 are secular hyperfine couplings between the electrons and the nucleus, and B_1 and B_2 are pseudo-secular hyperfine couplings between the electrons and the nucleus. d and J are the dipolar coupling and J-coupling between the two electrons, respectively. It is worth noting that in a MAS experiment, ω_{0S_1}, ω_{0S_2}, B_1, B_2 and d are time-dependent, ignoring the chemical shift anisotropy of the nucleus. The direct product basis set consists of eight states of the form $|IS_1S_2\rangle$ as illustrated in Figure 3c. Treating the pseudo-secular hyperfine coupling as a small perturbation, we write the Hamiltonian as

$$H = H^{(0)} + H^{(1)} \quad (2.2.2)$$

where $H^{(0)}$ is the unperturbed part and $H^{(1)}$ is the perturbation. $H^{(0)}$ is block diagonal and therefore can be written as direct sum of four 2×2 matrices, *i.e.*

$$H^{(0)} = H_{15} \oplus H_{23} \oplus H_{67} \oplus H_{48} \quad (2.2.3)$$

$H^{(1)}$ only connects the four center states. Consequently $H^{(1)}$ is reduced to a 4×4 matrix perturbing the four center states only.

$$H^{(1)} = H_{2367}{}^{(1)} = \begin{pmatrix} 0 & 0 & \frac{B_\Delta}{4} & 0 \\ 0 & 0 & 0 & -\frac{B_\Delta}{4} \\ \frac{B_\Delta}{4} & 0 & 0 & 0 \\ 0 & -\frac{B_\Delta}{4} & 0 & 0 \end{pmatrix} \quad (2.2.4)$$

where

$$B_\Delta = B_1 - B_2 \quad (2.2.5)$$

2.2.3. Level crossings

(a) Electron-microwave crossings: The electron-microwave crossing occurs when the applied microwave frequency is on resonance with one of the EPR transitions (single electron flip). In principle, diagonalization of the unperturbed Hamiltonian gives a good approximation of this type of level crossings. The electron-microwave crossings read

$$\omega_{\mu w} = \omega_{0S_{1(2)}} \pm A_{1(2)} \pm (d - J) \quad (2.2.6)$$

which can be approximated as

$$\omega_{\mu w} \approx \omega_{0S_{1(2)}} \quad (2.2.7)$$

In other words, the three-spin system can be treated as non-interacting, and therefore flipping of a single electron occurs when the microwave frequency matches the Larmor frequency of either electron.

(b) The electron-electron crossings: The electron-electron crossings occur in the {23} and {67} subspaces (Figure 3c). This can be realized by treating the d and J terms in H_{23} and H_{67} as perturbations. The avoided level crossings correspond to the degeneracy of these subspaces in the absence of the d and J perturbation. It follows that

$$\omega_\Delta = \mp \frac{A_\Delta}{2} \approx 0 \quad (2.2.8)$$

where

$$A_\Delta = A_1 - A_2 \quad (2.2.9)$$

$$\omega_\Delta = \omega_{0S_1} - \omega_{0S_2} \quad (2.2.10)$$

The signs in (2.2.8) correspond to the degeneracy in H_{23} and H_{67}, respectively.

We then use degenerate perturbation theory, resulting in *1:1* mixing of states in the {23} and {67} subspaces due to the electron-electron couplings. As a consequence, the two electrons exchange polarization at these level crossings (Figure 3c). The rate at which electrons exchange polarization at these level crossings can be approximated using Landau-Zener theory as demonstrated by Thurber *et al*. To see that the energy levels actually do not cross, hence the name *avoided level crossing*, we note that in the vicinity of the degeneracy point, H_{23} and H_{67} can be diagonalized analytically. For example, diagonalization of H_{23} gives the following eigenenergies

$$\tilde{E}_2 = \frac{1}{2}\left[\left(\omega_{0I} - \frac{D_d}{2}\right) \pm \sqrt{\left(\omega_\Delta + \frac{A_\Delta}{2}\right)^2 + D_0^2}\right] \quad (2.2.11)$$

$$\tilde{E}_3 = \frac{1}{2}\left[\left(\omega_{0I} - \frac{D_d}{2}\right) \mp \sqrt{\left(\omega_\Delta + \frac{A_\Delta}{2}\right)^2 + D_0^2}\right] \quad (2.2.12)$$

where

$$D_d = 2(d - J) \quad (2.2.13)$$

$$D_0 = -(d + 2J) \quad (2.2.14)$$

The + in (2.2.11) and − in (2.2.12) corresponds to positive $\omega_\Delta + A_\Delta/2$. Whereas, The − in (2.2.11) and + in (2.2.12) corresponds to negative $\omega_\Delta + A_\Delta/2$.

$$\lim_{\omega_\Delta + \frac{A_\Delta}{2} \to 0^+} \tilde{E}_2 = \lim_{\omega_\Delta + \frac{A_\Delta}{2} \to 0^-} \tilde{E}_3 = \frac{1}{2}\left[\left(\omega_{0I} - \frac{D_d}{2}\right) + D_0\right] \quad (2.2.15)$$

$$\lim_{\omega_\Delta + \frac{A_\Delta}{2} \to 0^-} \tilde{E}_2 = \lim_{\omega_\Delta + \frac{A_\Delta}{2} \to 0^+} \tilde{E}_3 = \frac{1}{2}\left[\left(\omega_{0I} - \frac{D_d}{2}\right) - D_0\right] \quad (2.2.16)$$

This means that the energy levels do not cross and the energy gap is approximately equal to the perturbation D_0 from the *e-e* couplings as demonstrated in Figure 3e.

(c) Three-spin crossings: In general this type of level crossing does not coincide with the electron-electron crossing, *i.e.* the condition (2.2.8) is not fulfilled. Let us assume that

$$\omega_\Delta \pm \frac{A_\Delta}{2} \geq 0 \quad (2.2.17)$$

In this case, the two energy levels at the center are

$$\tilde{E}_3 = \frac{1}{2}\left[\left(\omega_{0I} - \frac{D_d}{2}\right) - \sqrt{\left(\omega_\Delta + \frac{A_\Delta}{2}\right)^2 + D_0^2}\right] \quad (2.2.18)$$

$$\tilde{E}_6 = \frac{1}{2}\left[\left(-\omega_{0I} - \frac{D_d}{2}\right) + \sqrt{\left(\omega_\Delta - \frac{A_\Delta}{2}\right)^2 + D_0^2}\right] \quad (2.2.19)$$

Imposing the degeneracy of the two levels in (2.2.18) and (2.2.19), we obtain

$$\omega_{0I} = \frac{1}{2}\left[\sqrt{\left(\omega_\Delta + \frac{A_\Delta}{2}\right)^2 + D_0^2} + \sqrt{\left(\omega_\Delta - \frac{A_\Delta}{2}\right)^2 + D_0^2}\right] \quad (2.2.20)$$

This condition can be simplified for small A_Δ.

$$\omega_{0I} \approx \sqrt{\omega_\Delta^2 + D_0^2} \quad (2.2.21)$$

Note that the matching conditions in (2.2.20) and (2.2.21) were established without any assumption on the size of the e⁻-e⁻ dipolar and *J* couplings. For biradicals that have been used for CE, the e⁻-e⁻ dipolar coupling is 20–35 MHz; the *J* coupling is usually negligible except for the case of BTurea (~ 20 MHz). Therefore, we can assume that e⁻-e⁻ dipolar and *J* couplings are very small compared to the nuclear Larmor frequency. In this case, the condition (2.2.21) can be simplified further.

$$\omega_\Delta \approx \sqrt{\omega_{0I}{}^2 - D_0^2} \approx \omega_{0I} - \frac{D_0^2}{2\omega_{0I}} \approx \omega_{0I} \quad (2.2.22)$$

The *1:1* state mixing due to $H^{(1)}$ given in (2.2.4) arises from degenerate perturbation theory, resulting in the change in the nuclear polarization. Similar to the electron-electron avoided level crossings, the energy gap for this type of avoided level crossings is equal to *B* .

2.2.4. Paramagnet induced signal quenching—Another result associated with the MAS is the signal quenching effect due to the paramagnetic dopants. This was documented recently by Corzilius *et al.* [44] and Thurber *et al.* [54]. Corzilius *et al.* studied the effect of four different polarizing agents including both single (trityl-OX063, 4-amino TEMPO, Gd^{3+}-DOTA) and two electron (TOTAPOL) species. Figure 4a shows the signal losses during CP MAS and static experiments for both trityl and TOTAPOL. The signal quenching appears to associate with the enhanced spin-lattice relaxation (Figure 4b), which implies that the MAS modulation of the electron-nuclear dipole coupling is essential for the quenching. The signal quenching in CP MAS experiments could be due to: (i) the large shift in resonances of nuclei in close proximity with the magnetic dopants, (ii) the homogenous linebroadening originating from the modulation of the electron-nuclear coupling, and (iii) decrease in the CP efficiency as a consequence of the PRE effect on the $T_{1\rho}$ of ^1H.

The work by Thurber *et al.* only used cross effect radicals including biradical (TOTAPOL) and triradicals (DOTOPA-4OH and DOTOPA-Ethanol). A factor as large as ~6 in the signal loss was observed at very low temperature (~ 20K) and with sample spinning (Figure 4c). The effect at higher temperature (80 K) was smaller, consistent with the data from Corzilius *et al.* Using quantum mechanical simulations, the authors suggest that the signal loss is due to the cross effect in the absence of microwaves and that the effect is dependent on the electron spin diffusion.

3. Pulsed DNP

3.1. Pulsed DNP using low microwave power

3.1.1. DNP in the nuclear rotating frame (NRF DNP)—This class of pulsed DNP mechanisms does not impose a defined resonance condition on the microwave power, and thus can operate at low microwave power. Accordingly, for this type of pulsed DNP sequences the microwave field is treated as a small perturbation, as was the case of CW DNP.

DNP in the nuclear rotating frame (NRF DNP) is conveniently described as the solid effect in the NRF. By transforming to the nuclear rotating frame, the mixing of states is no longer dependent on the magnetic field, but rather on the RF field strength, thereby eliminating the unfavorable field dependence of the conventional (lab frame) SE. The idea was first utilized by Bloembergen and Sokorin in a nuclear spin system [55], then by Wind [56] and, most recently, by Farrar [57] in an electron-nuclear system.

The Hamiltonian in the lab frame assumes the form

$$H = \omega_{0S} S_z - \omega_{0I} I_z + \vec{S} \cdot \overset{\Rightarrow}{A} \cdot \vec{I} - 2\omega_{1I} \cos(\omega_{rf} t) I_x \quad (3.1.1)$$

In the nuclear rotating frame, after secular approximation with respect to I_z and redefining the transverse axis of spin S, the Hamiltonian simplifies to

$$H = \omega_{0S} S_z + B S_x I_z + A S_z I_z - \omega_{1I} I_x \quad (3.1.2)$$

where A and B are the secular and pseudo-secular hyperfine coupling, respectively. We have assumed that the RF field is on resonance with the nuclear Larmor frequency.

After a $-\pi/2$ rotation about I_y, the Hamiltonian is transformed to

$$H = \omega_{0S} S_z - B S_x I_x - A S_z I_x - \omega_{1I} I_z \quad (3.1.3)$$

As opposed to the lab frame SE DNP, NRF DNP does not require pseudo-secular hyperfine coupling. In other words, the secular approximation with respect to S_z is valid and the Hamiltonian can be truncated to

$$H = \omega_{0S} S_z - A S_z I_x - \omega_{1I} I_z \quad (3.1.4)$$

which is block diagonal in the direct product basis, and H is a direct sum of two *2×2* matrices.

$$H = H_{13} \oplus H_{24} \quad (3.1.5)$$

Diagonalization of H is straightforward, and the matching condition is given as

$$\Omega_S = \omega_{\mu w} - \omega_{0S} = \pm \sqrt{\omega_{1I}^2 + \left(\frac{A}{2}\right)^2} \quad (3.1.6)$$

The mixing of states in each electronic subspace is defined by an angle θ

$$\theta = \arctan\left(\frac{A}{2\omega_{1I}}\right) \quad (3.1.7)$$

The state mixing is due to the secular hyperfine coupling, which is inversely proportional to the RF field instead of B_0 and is much larger than that for the SE. On the other hand, the separation between the positive and the negative enhancement conditions are much narrower compared to the lab frame SE. This feature is illustrated in Figure 5a for trityl radical. Note that the peaks of the lab frame SE and the NRF DNP appear to be opposite, which can be explained by the fact that the sign of the enhancement of NRF DNP is also dependent on the phase of the RF field.

3.1.2. Dressed state solid effect (DSSE)—The dressed state solid effect (DSSE) uses an RF field to drive the polarization transfer. Thus, the RF field is treated as a small, harmonic, time-dependent perturbation. The microwave field acts to create an electron spin

dressed state, an analogy to the dressed atom states in optics [60]. In the microwave rotating frame, the Hamiltonian is written as

$$H = -\omega_{0I}I_z + \omega_{1S}S_x + AS_zI_z + BS_zI_x \quad (3.1.8)$$

After a secular approximation with respect to I_z, the Hamiltonian is truncated to

$$H = -\omega_{0I}I_z + AS_zI_z + \omega_{1S}S_x \quad (3.1.9)$$

which is block diagonal in the direct product basis set, *i.e.*,

$$H = H_{12} \oplus H_{34} \quad (3.1.10)$$

where H_{12} and H_{34} are the Hamiltonian in the nuclear spin up and spin down subspaces, respectively. After diagonalization, we obtain the following matching condition for the RF frequency

$$\Omega_{rf} = \omega_{rf} - \omega_{0I} = \pm\sqrt{\omega_{1S}^2 + \left(\frac{A}{2}\right)^2} \quad (3.1.11)$$

The matching condition (3.1.11) implies that during the DNP period the RF is applied far off resonance and the NMR signal is observed on resonance. Thus far, DSSE has only been observed indirectly via the loss of the electron polarization [59]. In the case of d_{21}-BDPA, the secular hyperfine coupling is negligible and the matching conditions can be simplified to

$$\Omega_{rf} = \pm\omega_{1S} \quad (3.1.12)$$

This explains the result in Figure 5b, as the peak position appears to be displaced linearly with respect to the microwave field strength.

3.2. Pulsed DNP using high microwave power

In contrast to NRF DNP and DSSE, the microwave fields in the cases of nuclear orientation via electron spin locking (NOVEL) and the integrated solid effect (ISE) can no longer be treated as small perturbations. Both NOVEL and ISE rely on matching the Hartman-Hahn condition between the microwave rotating frame ($\omega_{1S}/2\pi$) and the nuclear lab frame ($\omega_{0I}/2\pi$). Even though ISE also functions with low microwave power, it performs optimally at the Hartman-Hahn condition, which requires strong microwave fields. In both cases the polarization is transferred coherently by the electron-nuclear dipolar coupling on the submicrosecond time scale, about three orders of magnitude faster than in conventional ^{1}H-^{13}C/^{15}N CP experiments. Both sequences were initially developed for the preparation of polarized targets using photoexcited triplet states of pentacene doped into host crystals of naphthalene or *ortho*- or *para*-terphenyl (Figure 6a). In the original experiments, the source of polarization was a photoexcited triplet state of pentacene generated by a laser pulse (Figure 6b). More recently, we have used NOVEL to enhance ^{1}H polarization in samples of polystyrene doped with BDPA. As illustrated in Figure 7 the microwave field profile shows a sharp rise to a peak at $\omega_{1S} = \omega_{0I} = 15$MHz followed by a long tail. There is a hint of a second maximum in the data at ~30 MHz (second harmonic),

but it is not much above the S/N. Note that the breadth of the matching condition is broad, indicating that the electron couples strongly to the ^{1}H's in the lattice. Solid echoes were used to record the ^{1}H spectra, and the enhancement ε=100 was obtained with experiments at 300 K. In addition, we have performed similar experiments on systems containing nitroxide radicals and on frozen solutions of SA-BDPA and trityl. Therefore, the experiment appears to be robust and widely applicable even at this early stage.

3.2.1. Nuclear orientation via electron spin locking (NOVEL)—The NOVEL sequence is an electron-nuclear analogue of cross polarization (CP) in NMR. In a heteronuclear spin system such as ^{1}H-^{13}C, the separation in energy levels due to the difference in the gyromagnetic ratios inhibits the polarization transfer. In a CP experiment, the separation is removed in the doubly rotating frame, leading to a matching in the energy levels, and thus enabling the polarization transfer between nuclei via dipolar coupling. For an electron-nuclear system, the difference in gyromagnetic ratios is so large that matching in a double rotating frame is difficult. However, matching between the electron rotating frame and the nuclear lab frame is possible and also allows efficient polarization transfer and generation of z-polarization. This idea was mentioned in the original Hartman-Hahn paper on cross polarization [62] and was implemented on an electron-nuclear system by Wenckenbach *et al.* in a NOVEL experiment. In the next section, we derive the matching condition, and for a more detailed discussion on the NOVEL sequence we refer the readers to the papers by Wenckebach *et al.* [63; 64]

In the laboratory frame, the Hamiltonian for the NOVEL experiment has the form

$$H = \omega_{0S} S_z - \omega_{0I} I_z + \vec{S} \cdot \vec{\vec{A}} \cdot \vec{I} + 2\omega_{1S} \cos(\omega_{\mu w} t) S_x \quad (3.2.1)$$

where the first two terms are the Zeeman interactions, the third is the electron-nuclear interaction, and the last is the microwave spin lock field. Upon transforming to the microwave rotating frame, the Hamiltonian can be truncated to

$$H = \Omega_S S_z - \omega_{0I} I_{zz} + A_{zx} S_z I_x + A_{zy} S_z I_y + A_{zz} S_z I_z + \omega_{1S} S_x \quad (3.2.2)$$

where Ω_S is the microwave offset

$$\Omega_S = \omega_{0S} - \omega_{\mu w} \quad (3.2.3)$$

Transformation to a tilted frame that combines the first and the last terms yields

$$H = \omega_{eff} S_z - \omega_{0I} I_z + \left(A_{zx} I_x + A_{zy} I_y + A_{zz} I_z \right) \left(S_z \cos\theta - S_x \sin\theta \right) \quad (3.2.4)$$

where

$$\omega_{eff} = \pm \sqrt{\Omega_S^2 + \omega_{1S}^2} \quad (3.2.5)$$

The sign of ω_{eff} depends on the phase as well as the offset of the microwave.

We now redefine the transverse axes of the nuclear spin by combining the terms containing I_x and I_y yielding the Hamiltonian

$$H = \omega_{eff} S_z - \omega_{0I} I_z + (A I_z + B I_x)(S_z \cos\theta - S_x \sin\theta) \quad (3.2.6)$$

where A and B are secular and pseudo-secular hyperfine couplings, respectively.

$$A = A_{zz} \quad (3.2.7)$$

$$B = \sqrt{A_{zx}^2 + A_{zy}^2} \quad (3.2.8)$$

Using perturbation theory, we can write the Hamiltonian as

$$H = H^{(0)} + H^{(1)} \quad (3.2.9)$$

where the unperturbed Hamiltonian H_0 and the perturbation H_1 are given as

$$H^{(0)} = \omega_{eff} S_z - \omega_{0I} I_z + A\cos\theta I_z S_z \quad (3.2.10)$$

$$H^{(1)} = B I_x (S_z \cos\theta - S_x \sin\theta) - A\sin\theta I_z S_x \quad (3.2.11)$$

The inter-subspace splitting between the ZQ subspace and the DQ subspace is approximately ω_{0I}, which is very large compared to the perturbation even at a magnetic field as low as 0.35 T. On the other hand, if the matching condition is fulfilled, states in either the DQ or ZQ subspace are degenerate, resulting in a complete intra-subspace state mixing due to the perturbation, and thus leading to polarization transfer. The perturbation can be truncated to contain only DQ (flip-flip) and ZQ (flip-flop) terms as the following

$$H^{(1)} \approx B\sin\theta I_x S_x \quad (3.2.12)$$

For the positive ω_{eff}, the degeneracy in the DQ subspace leads to the matching condition

$$\omega_{0I} = \omega_{eff} = \sqrt{\Omega_S^2 + \omega_{1S}^2} \quad (3.2.13)$$

If the microwave offset is negligible, the matching condition is simplified to

$$\omega_{1S} \approx \omega_{0I} \quad (3.2.14)$$

which means that the nuclear Larmor frequency equals the Rabi frequency of the electron. In other words, nutation of the nucleus in the laboratory frame matches that of the electron in the rotating frame.

3.2.2. Integrated solid effect (ISE)—The ISE was originally developed as an improvement to the SE for cases in which the EPR spectrum is broad, and thus did not exclusively require high microwave power. In this case, the overlap of the positive and the negative SE (differential SE) limits the net DNP enhancement. The idea was to sweep the

magnetic field in such a manner so that different electron spin packets constructively contribute to the net DNP enhancement. The first experiment showed a 21-fold improvement compared to the regular SE. In subsequent experiments, ISE was performed while satisfying the Hartman-Hahn matching condition similar to the NOVEL sequence, which led to the name integrated cross polarization (ICP).

The Hamiltonian has the form

$$H = \omega_{0S}(t)S_z - \omega_{0I}(t)I_z + \vec{S} \cdot \overleftrightarrow{A} \cdot \vec{I} + 2\omega_{1S}\cos(\omega_{\mu w}t)S_x \quad (3.2.15)$$

The Zeeman terms are time dependent due to the magnetic field sweep.

In the microwave rotating frame, ignoring the time dependence in the nuclear Zeeman term

$$H = \Omega_S(t)S_z - \omega_{0I}I_z + A_{zx}S_zI_x + A_{zy}S_zI_y + A_{zz}S_zI_z + \omega_{1S}S_x \quad (3.2.16)$$

$$\Omega_S(t) = \omega_{0S}(t) - \omega_{\mu w} \quad (3.2.17)$$

And we obtain the following matching condition that is identical to the NOVEL matching condition

$$\omega_{0I}^2 = \Omega_S^2(t) + \omega_{1S}^2 \quad (3.2.18)$$

Solving for $\Omega_S(t)$

$$\Omega_S(t) = \pm\sqrt{\omega_{0I}^2 - \omega_{1S}^2} \quad (3.2.19)$$

The $\pm$ sign indicates that two electron spin packets located at $\omega_{0S} \pm \sqrt{\omega_{0I}^2 - \omega_{1S}^2}$ contribute constructively to the DNP enhancement as opposed to the destructive contribution of two spin packets located at $\omega_{0S}.\pm \omega_{0I}$ in the original solid effect. Furthermore, sweeping of the magnetic field allows participation of all electron spin packets in a broad EPR line to participate in the DNP process.

4. Applications to biological systems

Another important issue in biomolecular DNP is the loss of resolution that occurs in protein spectra at low temperatures. Although this is not directly related to the topic of "DNP mechanisms" discussed in the remainder of this review, it is of considerable importance to the development of the field, and we therefore consider it here.

The primary rationale for developing high field biomolecular DNP experiments is to provide a solution to the issue of low sensitivity that is a universal problem in NMR spectroscopy, and in MAS spectra in particular. Furthermore, it is now well established in several studies that DNP functions most efficiently at low temperatures, where the electronic and nuclear relaxation times are longer. For example, recent temperature dependent data shows that the enhancement obtained from a sample of ^{13}C-urea dispersed in TOTAPOL/glycerol/H$_2$O

mixtures doubles when the temperature is reduced from ~100 K to ~80 K [32]. However, in several studies of proteins, low temperatures have resulted in spectral broadening and a concomitant loss of spectral resolution. Thus, in order to optimize the benefit of DNP experiments, it is important to determine the factors that are leading to the loss of resolution and to develop methods for preparation of samples that maintain resolution at low temperatures. At the moment it appears that the optimal results are obtained with ^{13}C-^{15}N spectra of proteins that have a well defined structure and are resident in a preexisting matrix. In addition, there is evidence that high fields will improve resolution significantly. Some representative systems studied with DNP that illustrate these temperature dependent effects are small molecules (urea and proline are typical standards), small microcrystalline proteins (αspectrin-SH3[65]), membrane proteins in a native matrix (bacteriorhodopsin, bR [66–69], proteorhodopsin[70; 71]) or in an artificial lipid bilayer (M2$_{18–60}$ [72], neurotoxin[73]), amyloid fibrils (TTR$_{105–115}$ [74], PI3-SH3 [75]) or macromolecular complexes such as needle proteins [76], ribosomal particles[77], or virus particles[78].

In essentially all of these experiments, it is necessary to disperse the system in glycerol/H$_2$O solvent for two reasons. First, a glycerol/H$_2$O mixture is cryoprotectant that forms a glass, thereby preventing ice crystal formation and protecting the protein from cold denaturation. Second, it simultaneously disperses the paramagnetic polarizing agent, preventing formation of microcrystals of the polarizing agent, so that DNP functions optimally. The requirement for cryoprotection is well established from low temperature X-ray crystallography, and the necessity of dispersing the polarizing agent in a glass is known from EPR experiments. Since samples for MAS experiments are frozen slowly, it is customary to use ~60%/40% glycerol/water solutions since they always form a glass regardless of the cooling rate [79; 80]. In an MAS experiment the rotor accounts for ~50–75% of the heat capacity of the sample and the sample itself freezes via contact with the cold rotor walls. Since sapphire has a high thermal conductivity at low temperatures, it is desirable to use that material rather than ZrO$_2$ for DNP experiments. In X-ray crystallography the glycerol concentration is lower since the samples have a small heat capacity and freeze rapidly.

At the moment it is not clear that there is a generally applicable approach to deal with the loss of resolution at low temperatures, but there are some tantalizing hints in spectra published by several groups involved in high frequency DNP experiments. First, in some of the initial DNP MAS protein spectra of bR photocycle intermediates recorded at ~90 K and 380 MHz/250 GHz that were published, the resolution of the retinal-Schiff peaks was ~1 ppm in ^{13}C-^{15}N spectra. These results are documented in several publications [66–69] and discussed elsewhere [81] so we refer the reader to those references. However, the salient feature of bR is that it is a protein in its native "purple membrane" environment. Second, Gelis, et al. [77] demonstrated that peptides such as the factor IF-1 bound to ribosomal particles (E30S) (a 800 kDa complex) yield well resolved spectra when specifically labeled Tyr, His and Lys residues are examined in 2D ^{13}C-^{15}N spectra. Again this is a system where the ribosomal particle has a structure that remains intact at low temperatures. The well resolved cross peaks from Lys, Thr and Ala residues present in ^{13}C-^{15}N spectra are illustrated in Figure 8.

Finally, PI3-SH3 amyloid fibrils exhibit resolved cross peaks in ^{13}C-^{15}N ZF-TEDOR [75] and the fibril structure provides a lattice for the proteins. It is worth mentioning that ^{13}C-^{13}C spectra of these systems that were recorded at 380 or 400 MHz ^{1}H frequencies exhibit aliphatic regions that are broadened and resemble the results from $A\beta_{1-40}$, Illustrated in Figure 9a below. In contrast, the ^{13}C-^{15}N spectra are well resolved and yield important information. Thus, if the spectroscopy is confined to low frequencies, ~ 400 MHz, then it appears that the optimal resolution is available from the ^{13}C-^{15}N rather than ^{13}C-^{13}C spectra.

A second possible approach to increasing the resolution is to move the experiments to higher fields. This is illustrated in Figure 9 with spectra from del Amo et al. that shows spectra of $A\beta_{1-40}$ fibrils at 400, 600 and 850 MHz ^{1}H frequencies and a remarkable increase in resolution with operating field. In particular, the aliphatic region which is broadened at 400 MHz is progressively more well resolved at higher fields, especially at 850 MHz. A second example illustrating this behavior is shown in Figure 10 that is the PDSD spectrum obtained from MixH needles at 600 MHz/14.1T and again shows remarkable resolution at 100 K. The broad aliphatic region between 20–70 ppm is much reduced, but much of the rest of the spectrum is resolved. This is currently the most well resolved low temperature DNP spectrum present in the literature, and it would be interesting to examine similar systems at higher and lower fields to establish the effect of B_0 on resolution. Finally, a third example of the field effect was recently reported in spectra of a virus particle. In particular, the 400 MHz spectra resemble those in Figure 9a but at 800 MHz they are well resolved [78]. These results suggest, but do not prove, that at low temperatures the ^{13}C-^{13}C couplings in the aliphatic region assume increased homogeneous character that does not narrow with MAS, an effect discussed by Maricq and Waugh [83]. At the higher field where the chemical shift difference is larger, the flipflop terms in the Hamiltonian are truncated and the inhomogeneous character is restored and the spectra narrow with MAS. Clearly, this is an area ripe for investigation and as higher field DNP instruments become more common, additional data will permit further elucidation of these effects. In addition, the possibility of NMR spectrometers operating at 1.2–1.3 GHz ^{1}H Larmor frequencies or 28.2–30.5 T is on the horizon [84], and these instruments could further improve the resolution of low temperature spectra.

5. Summary

In summary we have seen that there are now well established methods to perform biomolecular MAS DNP experiments. Perhaps the most successful approach has involved the CE together with nitroxide biradicals. Thus, using AMUPol as a polarizing agent we have achieved enhancement of 400 at 380 MHz/250 GHz and further improvements seem likely. This approach has been used to polarize a variety of biomolecular samples and will likely continue to be important in future experiments. However, in the last few years it has become clear that other mechanisms could be important for high field DNP depending on the availability of suitable polarizing agents and instrumentation. For example, the recently discovered Overhauser effect in insulating solids appears to scale favorably with B_0 and, with polarizing agents that exhibit larger hyperfine couplings, it could become the method of choice for high field CW experiments. In addition, the data in the literature to date appears

to indicate that DNP at higher magnetic fields will offer higher resolution due to the dispersion of chemical shifts and truncation of homogeneous couplings that are present in the spectra. Finally, it is possible to perform time domain DNP experiments and these approaches should not exhibit the field dependence displayed by CW methods like the CE or SE. However, implementing pulsed DNP methods will likely require the development of new instrumentation, namely gyroamplifiers, and new methods for time domain polarization transfer. When these become available we anticipate that pulsed DNP will become the method of choice for electron-nuclear polarization transfer.

Acknowledgments

References

1. Overhauser AW. Polarization of Nuclei in Metals. Physical Review. 1953; 92:411.

2. Carver TR, Slichter CP. Polarization of Nuclear Spins in Metals. Physical Review. 1953; 92:212.

3. Carver TR, Slichter CP. Experimental Verification of the Overhauser Nuclear Polarization Effect. Physical Review. 1956; 102:975.

4. Jefferies CD. Polarization of Nuclei by Resonance Saturation in Paramagnetic Crystals. Physical Review. 1957; 106:164–165.

5. Jefferies CD. Dynamic Orientation of Nuclei by Forbidden Transitions in Paramagnetic Resonance. Physical Review. 1960; 117:1056–1069.

6. Abragam A, Proctor WG. C R Acad Sci. 1958; 246:2253.

7. Erb E, Motchane JL, Uebersfeld J. C R Acad Sci. 1958; 246:2121.

8. Kessenikh AV, Lushchikov VI, Manenkov AA, Taran YV. Proton Polarization in Irradiated Polyethylenes. Soviet Physics – Solid State. 1963; 5:321–329.

9. Kessenikh AV, Manenkov AA, Pyatnitskii GI. On Explanation of Experimental Data on Dynamic Polarization of Protons in Irradiated Polyethylenes. Soviet Physics – Solid State. 1964; 6:641–643.

10. Hwang CF, Hill DA. Phenomenological Model for the New Effect in Dynamic Polarization. Physical Review Letters. 1967; 19:1011.

11. Hwang CF, Hill DA. New Effect in Dynamic Polarization. Physical Review Letters. 1967; 18:110.

12. Wollan DS. Dynamic nuclear polarization with an inhomogeneously broadened ESR line. I. Theory. Physical Review B: Condensed Matter. 1976; 13:3671.

13. Wollan DS. Dynamic nuclear polarization with an inhomogeneously broadened ESR line. II. Experiment. Physical Review B: Condensed Matter. 1976; 13:3686.

14. Abragam A, Goldman M. Principles of dynamic nuclear polarization. Rep Prog Phys. 1978; 41:395–467.

15. Atsarkin VA. Dynamic Polarization of Nuclei in Solid Dielectrics. Soviet Physics Solid State. 1978; 21:725–744.

16. Abragam, A.; Goldman, M. Nuclear Magnetism: Order and Disorder. Clarendon Press; Oxford: 1982.

17. Atsarkin VA, Kessenikh AV. Dynamic Nuclear Polarization in Solids: The Birth and Development of the Many-Particle Concept. Appl Magn Reson. 2012; 43:7–19.

18. Wind RA, Duijvestijn MJ, van der Lugt C, Manenschijn A, Vriend J. Applications of Dynamic Nuclear-Polarization in C-13 NMR in Solids. Progress in Nuclear Magnetic Resonance Spectroscopy. 1985; 17:33–67.

19. Maresch GG, Kendrick RD, Yannoni CS, Galvin ME. Dynamic Nuclear Polarization via Confined Electrons in Bulk Solids. Jour Magnetic Resonance. 1989; 82:41–50.

20. Singel DJ, Seidel H, Kendrick RD, Yannoni CS. A Spectrometer for EPR, DNP, and Multinuclear High-Resolution NMR. Journal of Magnetic Resonance. 1989; 81:145–161.

21. Yannoni CS, Myhre PC, Webb GG. Magic angle spinning nuclear magnetic resonance near liquid-helium temperatures. Variable-temperature CPMAS spectra of the 2-norbornyl cation to 6 K. J Am Chem Soc. 1990; 112:8991–8992.

22. Afeworki M, Schaefer J. Mechanism of DNP-Enhanced Polarization Transfer across the Interface of Polycarbonate/Polystyrene Heterogeneous Blends. Macromolecules. 1992; 25:4092–4096.

23. Hu JZ, Zhou J, Yang B, Li L, Qiu J, Ye C, Solum MS, Wind RA, Pugmire RJ, Grant DM. Dynamic nuclear polarization of nitrogen-15 in benzamide. Solid State Nuclear Magnetic Resonance. 1997; 8:129–137. [PubMed: 9203286]

24. Becerra L, Gerfen G, Temkin R, Singel D, Griffin R. Dynamic nuclear polarization with a cyclotron resonance maser at 5 T. Physical Review Letters. 1993; 71:3561–3564. [PubMed: 10055008]

25. Becerra LR, Gerfen GJ, Bellew BF, Bryant JA, Hall DA, Inati SJ, Weber RT, Un S, Prisner TF, McDermott AE, Fishbein KW, Kreischer K, Temkin RJ, Singel DJ, Griffin RG. A Spectrometer for Dynamic Nuclear Polarization and Electron Paramagnetic Resonance at High Frequencies. Journal of Magnetic Resonance. 1995; A117:28–40.

26. Bajaj V, Farrar C, Hornstein M, Mastovsky I, Vieregg J, Bryant J, Elena B, Kreischer K, Temkin R, Griffin R. Dynamic nuclear polarization at 9T using a novel 250GHz gyrotron microwave source. J Magn Reson. 2003; 160:85–90. [PubMed: 12615147]

27. Rosay M, Tometich L, Pawsey S, Bader R, Schauwecker R, Blank M, Borchard PM, Cauffman SR, Felch KL, Weber RT, Temkin RJ, Griffin RG, Maas WE. Solid-state dynamic nuclear polarization at 263 GHz: spectrometer design and experimental results. Physical Chemistry Chemical Physics. 2010; 12:5850–5860. [PubMed: 20449524]

28. Barnes A, Markhasin E, Daviso E, Michaelis V, Nanni EA, Jawla SK, Mena EL, DeRocher R, Thakkar A, Woskov PP, Herzfeld J, Temkin RJ, Griffin RG. Dynamic nuclear polarization at 700 MHz/460 GHz. J Magn Reson. 2012; 224:1–7. [PubMed: 23000974]

29. Hu K-N, Debelouchina GT, Smith AA, Griffin RG. Quantum mechanical theory of dynamic nuclear polarization in solid dielectrics. Journal of Chemical Physics. 2011; 134

30. Mentink-Vigier F, Akbey U, Hovav Y, Vega S, Oschkinat H, Feintuch A. Fast passage dynamic nuclear polarization on rotating solids. Journal of magnetic resonance (San Diego, Calif : 1997). 2012; 224:13–21.

31. Thurber K, Tycko R. Theory for cross effect dynamic nuclear polarization under magic angle spinning in solid state nuclear magnetic resonance: the importance of level crossings. J Chem Phys. 2012; 137:084508–1. [PubMed: 22938251]

32. Ni QZ, Daviso E, Can TV, Markhasin E, Jawla SK, Swager TM, Temkin RJ, Herzfeld J, Griffin RG. High Frequency Dynamic Nuclear Polarization. Accounts of Chemical Research. 2013; 46:1933–1941. [PubMed: 23597038]

33. Barnes AB, De Paëpe G, van der Wel PCA, Hu KN, Joo CG, Bajaj VS, Mak-Jurkauskas ML, Sirigiri JR, Herzfeld J, Temkin RJ, Griffin RG. High-Field Dynamic Nuclear Polarization for Solid and Solution Biological NMR. Applied Magnetic Resonance. 2008; 34:237–263. [PubMed: 19194532]

34. Maly T, Debelouchina GT, Bajaj VS, Hu K-N, Joo C-G, Mak-Jurkauskas ML, Sirigiri JR, van der Wel PCA, Herzfeld J, Temkin RJ, Griffin RG. Dynamic nuclear polarization at high magnetic fields. The Journal of Chemical Physics. 2008; 128:052211–19. [PubMed: 18266416]

35. Nanni EA, Barnes AB, Griffin RG, Temkin RJ. THz Dynamic Nuclear Polarization NMR. IEEE Transactions on Terahertz Science and Technology. 2011; 1:145–163. [PubMed: 24639915]

36. Can TV, Caporini MA, Mentink-Vigier F, Corzilius B, Walish JJ, Rosay M, Maas WE, Baldus M, Vega S, Swager TM, Griffin RG. Overhauser effects in insulating solids. Journal of Chemical Physics. 2014; 141

37. Goldman, M. Spin Temperature and Nuclear Magnetic Resonance in Solids. Oxford University Press; 1970.

38. Corzilius B, Smith AA, Griffin RG. Solid effect in magic angle spinning dynamic nuclear polarization. J Chem Phys. 2012

39. Smith AA, Corzilius B, Barnes AB, Maly T, Griffin RG. Solid effect dynamic nuclear polarization and polarization pathways. Journal of Chemical Physics. 2012; 136:015101. (1–16). [PubMed: 22239801]

40. Corzilius B, Smith AA, Barnes AB, Luchinat C, Bertini I, Griffin RG. High-Field Dynamic Nuclear Polarization with High-Spin Transition Metal Ions. Journal of the American Chemical Society. 2011; 133:5648–5651. [PubMed: 21446700]

41. Hu K-N, Song C, Yu H-h, Swager TM, Griffin RG. High-frequency dynamic nuclear polarization using biradicals: A multifrequency EPR lineshape analysis. The Journal of Chemical Physics. 2008; 128:052302–17. [PubMed: 18266419]

42. Hu KH, Yu H, Swager T, Griffin R. Dynamic nuclear polarization with biradicals. Journal of the American Chemical Society. 2004; 126:10844–5. [PubMed: 15339160]

43. Sauvee C, Rosay M, Casano G, Aussenac F, Weber RT, Ouari O, Tordo P. Highly Efficient, Water-Soluble Polarizing Agents for Dynamic Nuclear Polarization at High Frequency. Angewandte Chemie-International Edition. 2013; 52:10858–10861.

44. Corzilius B, Andreas LB, Smith AA, Ni QZ, Griffin RG. Paramagnet induced signal quenching in MAS-DNP experiments in frozen homogeneous solutions. Journal of Magnetic Resonance. 2014; 240:113–123. [PubMed: 24394190]

45. Shimon D, Hovav Y, Feintuch A, Goldfarb D, Vega S. DNP in the Solid State: A Transition between the Cross Effect and the Solid Effect. Phys Chem Chem Phys. 2012

46. Shimon D, Feintuch A, Goldfarb D, Vega S. Static H-1 dynamic nuclear polarization with the biradical TOTAPOL: a transition between the solid effect and the cross effect. Physical Chemistry Chemical Physics. 2014; 16:6687–6699. [PubMed: 24585094]

47. Hovav Y, Feintuch A, Vega S. Theoretical aspects of dynamic nuclear polarization in the solid state – spin temperature and thermal mixing. Physical Chemistry Chemical Physics. 2013; 15:188–203. [PubMed: 23160533]

48. Maly T, Miller A-F, Griffin RG. In situ High-Field Dynamic Nuclear Polarization-Direct and Indirect Polarization of 13C nuclei. ChemPhysChem. 2010; 11:999–1001. [PubMed: 20169604]

49. Maly T, Andreas LB, Smith AA, Griffin RG. 2H-DNP-enhanced 2H–13C solid-state NMR correlation spectroscopy. Phys Chem Chem Phys. 2010; 12:5872–5878. [PubMed: 20458422]

50. Michaelis VK, Corzilius B, Smith AA, Griffin RG. Dynamic Nuclear Polarization of O-17: Direct Polarization. Journal of Physical Chemistry B. 2013; 117:14894–14906.

51. Zagdoun A, Casano G, Ouari O, Lapadula G, Rossini AJ, Lelli M, Baffert M, Gajan D, Veyre L, Maas WE, Rosay MM, Weber RT, Thieuleux C, Coperet C, Lesage A, Tordo P, Emsley L. A slowly relaxing rigid biradical for efficient DNP surface enhanced NMR spectroscopy: expeditious characterization of functional group manipulation in hybrid materials. J Am Chem Soc. 2012

52. Zagdoun A, Casano G, Ouari O, Schwarzwalder M, Rossini AJ, Aussenac F, Yulikov M, Jeschke G, Coperet C, Lesage A, Tordo P, Emsley L. Large Molecular Weight Nitroxide Biradicals Providing Efficient Dynamic Nuclear Polarization at Temperatures up to 200 K. Journal of the American Chemical Society. 2013; 135:12790–12797. [PubMed: 23961876]

53. Hu, KN. Polarizing Agents for High-Frequency Dynamic Nuclear Polarization – Development and Applications. Chemistry, MIT; 2006. p. 274

54. Thurber KR, Tycko R. Perturbation of nuclear spin polarizations in solid state NMR of nitroxide-doped samples by magic-angle spinning without microwaves. Journal of Chemical Physics. 2014; 140

55. Bloembergen N, Sorokin PP. Nuclear Magnetic Resonance in the Cesium Halides. Physical Review. 1958; 110:865.

56. Wind RA, Li L, Lock H, Maciel GE. Dynamic nuclear polarization in the nuclear rotating frame. Journal of Magnetic Resonance. 1988; 79:577–582.

57. Farrar C, Hall D, Gerfen G, Rosay M, Ardenkjaer-Larsen J, Griffin R. High-frequency dynamic nuclear polarization in the nuclear rotating frame. J Magn Reson. 2000; 144:134–41. [PubMed: 10783283]

58. Hu K, Bajaj V, Rosay M, Griffin R. High-frequency dynamic nuclear polarization using mixtures of TEMPO and trityl radicals. J Chem Phys. 2007; 126:044512. [PubMed: 17286492]

59. Weis V, Bennati M, Rosay M, Griffin RG. Solid effect in the electron spin dressed state: A new approach for dynamic nuclear polarization. J Chem Phys. 2000; 113:6795–6802.

60. Mollow BR. Power Syectrum of Light Scattered by Two-Level Systems. Phys Rev. 1969; 188:1969–1975.

61. van den Heuvel DJ, Henstra A, Lin T-S, Schmidt J, Wenckebach WT. Transient oscillations in pulsed dynamic nuclear polarization. Chemical Physics Letters. 1992; 188:194–200.

62. Hartmann SR, Hahn EL. Nuclear Double Resonance in the Rotating frame. Phys Rev. 1962; 128:2042–2053.

63. Henstra A, Lin T-S, Schmidt J, Wenckeback WT. High Dynamic Nucler Polarization at Room Temperature. Chem Phys Letters. 1990; 165:6–10.

64. Henstra A, Wenckebach W. The theory of nuclear orientation via electron spin locking (NOVEL). Molecular Physics. 2008; 106:859–871.

65. Linden A, Franks WT, Akbey Ü, Lange S, van Rossum B-J, Oschkinat H. Cryogenic temperature effects and resolution upon slow cooling of protein preparations in solid state NMR. Journal of Biomolecular NMR. 2011:1–10.

66. Bajaj VS, Mak-Jurkauskas ML, Belenky M, Herzfeld J, Griffin RG. Functional and shunt states of bacteriorhodopsin resolved by 250-GHz dynamic nuclear polarization-enhanced solid-state NMR. Proc Nat'l Acad Sci. 2009; 106:9244–49. [PubMed: 19474298]

67. Bajaj VS, Mak-Jurkauskas ML, Belenky M, Herzfeld J, Griffin RG. DNP Enhanced Frequency-Selective TEDOR Experiments in Bacteriorhodopsin. Jour Magnetic Resonance. 2010; 202:9–13.

68. Barnes AB, Corzilius B, Mak-Jurkauskas ML, Andreas LB, Bajaj VS, Matsuki Y, Belenky ML, Lugtenburg J, Sirigiri JR, Temkin RJ, Herzfeld J, Griffin R. Resolution and polarization distribution in cryogenic DNP/MAS experiments. Phys Chem Chem Phys. 2010; 12

69. Mak-Jurkauskas ML, Bajaj VS, Hornstein MK, Belenky M, Griffin RG, Herzfeld J. Gradual Winding of the Bacteriorhodopsin Chromophore in the First Half of Its Ion-Motive Photocycle: a Dynamic Nuclear Polarization Enhanced Solid State NMR Study. Proc Nat'l Acad Sci. 2008; 105:883–888. [PubMed: 18195364]

70. Mao J, Do N-N, Scholz F, Reggie L, Mehler M, Lakatos A, Ong Y-S, Ullrich SJ, Brown LJ, Brown RCD, Becker-Baldus J, Wachtveitl J, Glaubitz C. Structural Basis of the Green–Blue Color Switching in Proteorhodopsin as Determined by NMR Spectroscopy. J Am Chem Soc. 2014; 136:17578–17590. [PubMed: 25415762]

71. Jakdetchai, Orawan; Denysenkov, V.; Becker-Baldus, J.; Dutagaci, B.; Prisner, TF.; Glaubitz, C. Dynamic Nuclear Polarization-Enhanced NMR on Aligned Lipid Bilayers at Ambient Temperature. J Am Chem Soc. 136:15533–15536. [PubMed: 25333422]

72. Andreas LB, Barnes AB, Corzilius B, Chou JJ, Miller EA, Caporini M, Rosay M, Griffin RG. Dynamic Nuclear Polarization Study of Inhibitor Binding to the M2 Proton Transporter from Influenza A. Biochemistry. 2013; 52:2774–2782. [PubMed: 23480101]

73. Linden AH, Lange S, Franks WT, Akbey U, Specker E, Rossum BJv, Oschkinat H. Neurotoxin II Bound to Acetylcholine Receptors in Native Membranes Studied by Dynamic Nuclear Polarization NMR. J Amer Chem Soc. 2011; 133:19266–19269. [PubMed: 22039931]

74. Debelouchina GT, Bayro MJ, Fitzpatrick AW, Ladizhansky V, Colvin MT, Caporini MA, Jaroniec CP, Bajaj VS, Rosay M, MacPhee CE, Vendruscolo M, Maas WE, Dobson CM, Griffin RG. Higher Order Amyloid Fibril Structure by MAS NMR and DNP Spectroscopy. J Amer Chem Soc. 2013; 135:19237–19247. [PubMed: 24304221]

75. Bayro MJ, Debelouchina GT, Eddy MT, Birkett NR, MacPhee CE, Rosay M, Maas WE, Dobson CM, Griffin RG. Intermolecular structure determination of amyloid fibrils with magic-angle spinning, dynamic nuclear polarization NMR. J Am Chem Soc. 2011; 133:13967–13974. [PubMed: 21774549]

76. Fricke P, Demers J-P, Becker S, Lange A. Studies on the MxiH Protein in T3SS Needles Using DNP-Enhanced ssNMR Spectroscopy. ChemPhysChem. 2014; 15:57–60. [PubMed: 24282046]

77. Gelis I, Vitzthum V, Dhimole N, Caporini MA, Schedlbauer A, Carnevale D, Connell SR, Fucini P, Bodenhausen G. Solid-state NMR enhanced by dynamic nuclear polarization as a novel tool for ribosome structural biology. J Biomol NMR. 2013; 56:85–93. [PubMed: 23689811]

78. Pintucda G, Lesage A, Emsley L. DNP experiments on a virus particle. 2015

79. Kalisky O, Ottolenghi M, Honig B, Korenstein R. Environmental Effects on the Formation and Photoreaction of the M412 Photoproduce of Bacteriorhodopsin – Implication for the Mechanism of Proteon Pumping. Biochemistry. 1981; 20:649–655. [PubMed: 7213600]

80. Baudot A, Alger L, Boutron P. Glass-Forming Tendency in the System Water–Dimethyl Sulfoxide. Cryobiology. 2000; 40:151–158. [PubMed: 10788314]

81. Mak-Jurkauskas M, Griffin RG. High Frequency Dynamic Nuclear Polarization. Encyclopedia of Nuclear Magnetic Resonance. 2010:159–174.

82. del Amo JML, Schneider D, Loquet A, Lange A, Reif B. Cryogenic solid state NMR studies of fibrils of the Alzheimer's disease amyloid-beta peptide: perspectives for DNP. Journal of Biomolecular NMR. 2013; 56:359–363. [PubMed: 23793606]

83. Maricq MM, Waugh JS. NMR in Rotating Solids. J Chem Phys. 1979; 70:3300.

84. Bascuñán J, Hahn S, Kim Y, Song J, Iwasa Y. 90-mm/18.8-T All-HTS Insert Magnet for 1.3 GHz LTS/HTS NMR Application: Magnet Design and Double-Pancake Coil Fabrication. IEEE Trans on Applied Superconductivity. 24:4300904.

Highlights

- Overhauser effect exists in insulating solids and appears to scale with B_0

- Cross effect DNP gives an enhancement of 400 at 9 T using AMUPol biradical

- Pulsed DNP on samples dope with BDPA or nitroxide radicals gives enhancement as high as 100
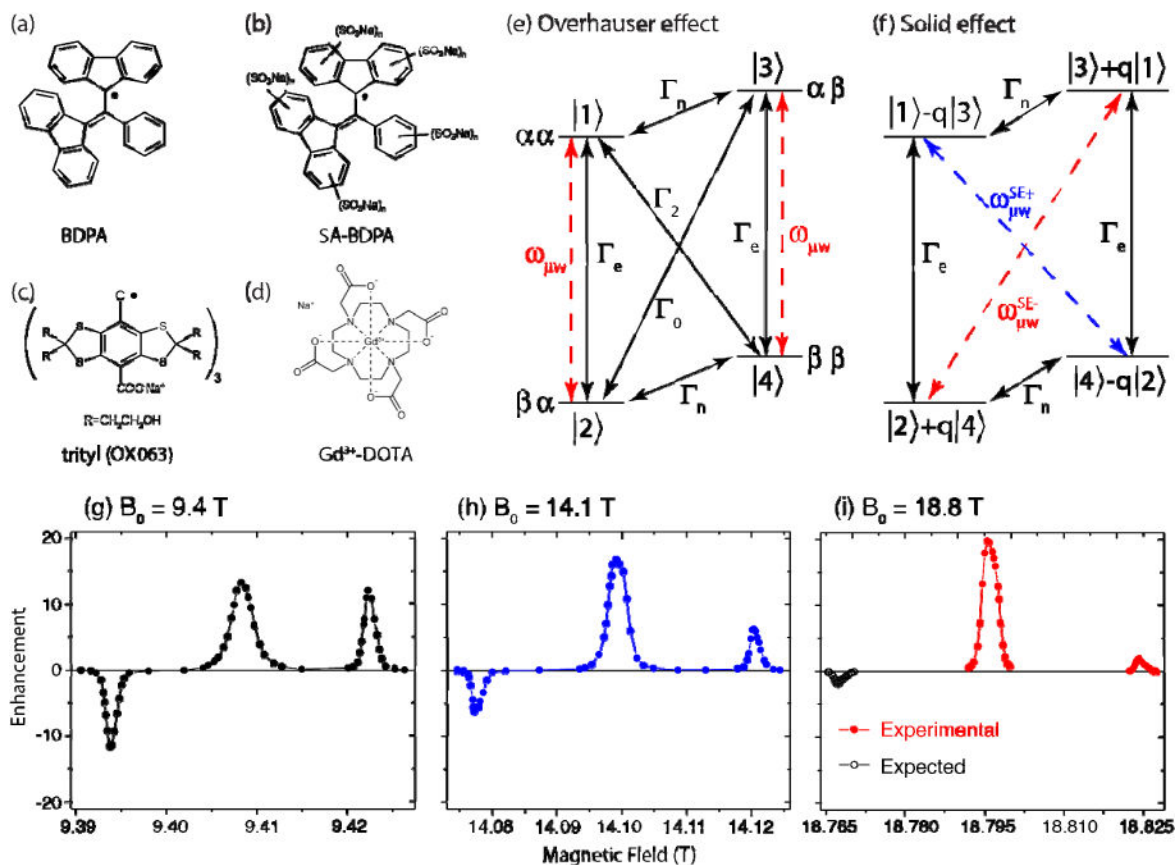
Figure 1.
Molecular structures of radicals for the solid effect (a) BDPA, (b) sulfonated BDPA (SA-BDPA), (c) trityl-OX063 and (d) Gd^{3+}-DOTA.

(e) Energy level diagram for the Overhauser effect. The imbalance between the ZQ and DQ relaxation rates act to distribute the polarizations upon the microwave driven saturation of the EPR transition, resulting in the DNP enhancement. (f) Energy level diagram for the solid effect. Neither the ZQ or DQ relaxations are required. Instead, saturation of the ZQ or DQ transitions leads to the DNP enhancement.

[1]H DNP enhancement Zeeman field profiles of BDPA in polystyrene are shown for (g) 9.4 T, (h) 14.1 T and (i) 18.8 T [36]. The positive enhancement due to the Overhauser effect is present at the center of each field profile and appears to scale with B_0. In contrast, the solid effect enhancements scales very closely to B_0^{-2}. At 18.8 T, the maximum enhancement of the Overhauser effect is one order of magnitude larger than that of the solid effect.
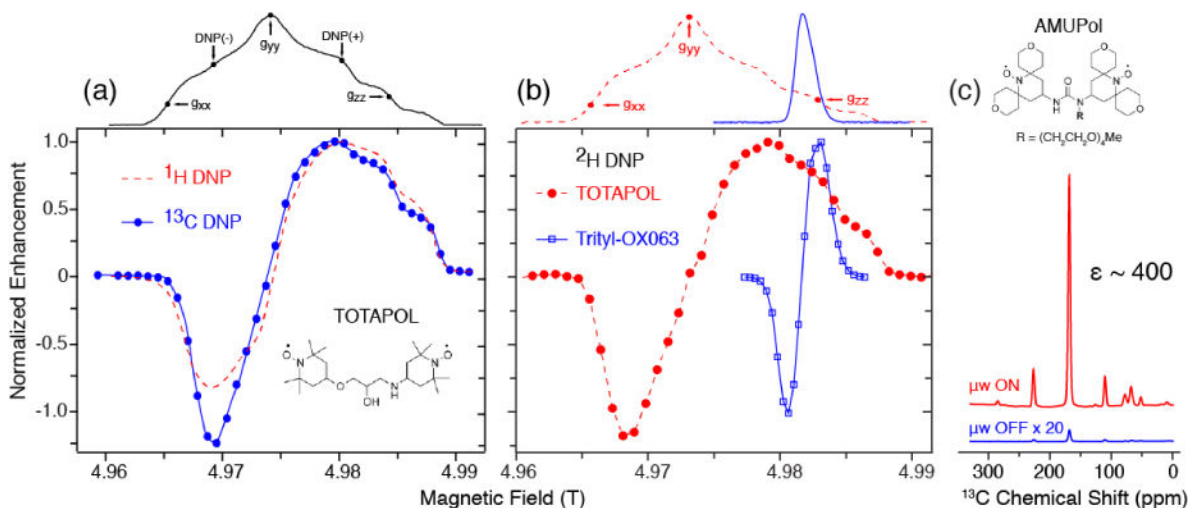
Figure 2.
(a) ^{1}H and ^{13}C DNP field profiles of TOTAPOL. (b) ^{2}H DNP field profiles of TOTAPOL and trityl-OX063. For TOTAPOL, the maximum ^{1}H enhancement is obtained at the DNP(+) field position, whereas for other nuclei of lower gyromagnetic ratios such as ^{13}C and ^{2}H, the maximum enhancements are at the DNP(−) field position. In both cases, the asymmetry is ~ 20%. For low gamma nuclei, trityl-OX03, a narrow-line radical, still satisfies the CE condition and gives higher enhancement by a factor of ~ 4 compared to TOTAPOL. (c) Cross effect DNP at 380 MHz/250 GHz using biradical AMUPol. The sample contains 1 M ^{13}C, ^{15}N-urea in 60/30/10 (volume ratio) d8-glycerol/D_2O/H_2O glassy matrix doped with 10 mM AMUPol. We obtained an enhancement of 400 at 80 K. To date, AMUPol is the best biradical for CE DNP. The radical also gives significant enhancement at temperatures above 150 K. Figures (a) and (b) are from Maly *et al.*[48] [49].
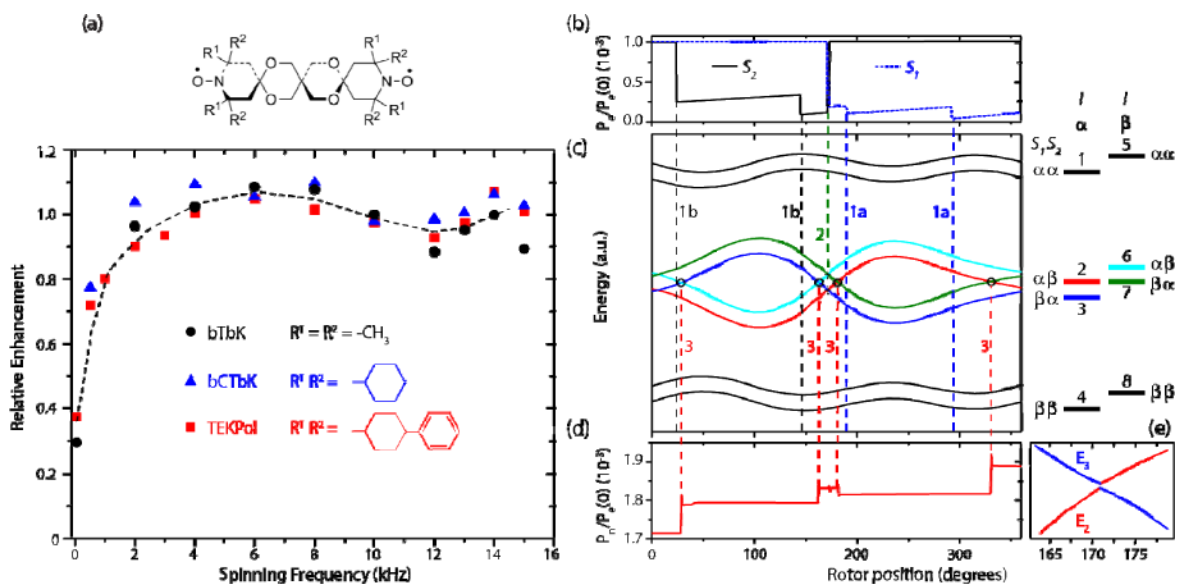
Figure 3.

Cross effect DNP in a three-spin system consisting of two electrons S_1, S_2 and one nuclear spin I. (a) Enhancement as a function of the spinning frequency on bTbK, bCTbK and TEKPol biradicals [52]. All three radicals show a similar trend with a local minimum at ~ 12 kHz, and appear to increase at faster spinning. (b) Polarization of electrons during one rotor period. (c) The modulations of the energy levels during one rotor period due to anisotropic interactions including the *g*-anisotropy and the e-e dipolar coupling. (d) Nuclear polarization during one rotor period. (e) Electron-electron avoided level crossing.

The dashed lines 1a and 1b indicate the flipping of the electron spins as the microwave frequency crosses one of the electron Larmor frequencies. The green dashed line 2 corresponds to the electron-electron avoided level crossing where the two electrons exchange their polarizations. The red dashed line 3 represents the three-spin avoided crossings at which DNP transfer occurs, as seen in the change of the nuclear polarization. Figures (b) to (e) were reproduced with slight modifications from the simulations by Mentink-Vigier *et al.* [30].
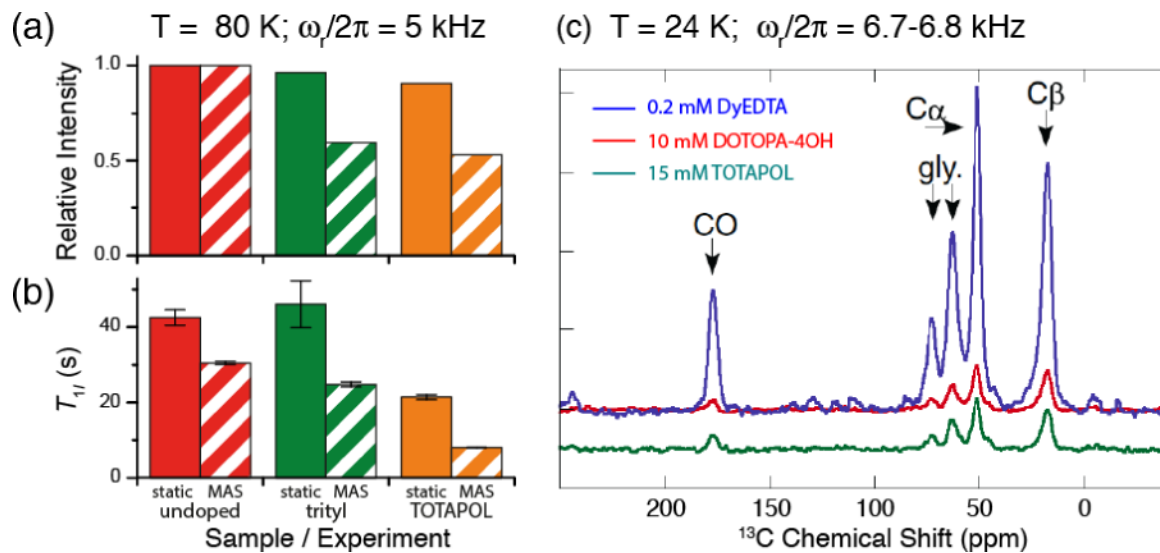
Figure 4.
(a) Signal quenching in homogenous frozen DNP samples induced by the paramagnetic dopants [36]. (b) T_1 of ^{1}H appears to correlate with signal quenching effect [36]. (c) CE in the absent of microwave acts to reduce the NMR signal [54]. This effect was observed at very low temperature.
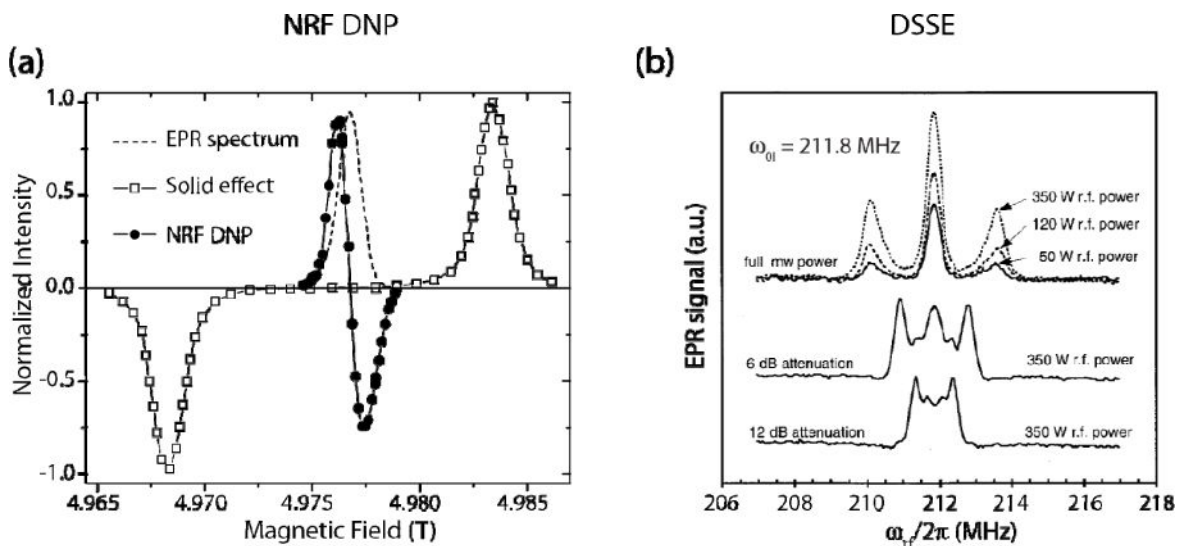
Figure 5.

(a) EPR spectrum (dashed), SE DNP (open square) and NRF DNP (solid circle) field profiles of trityl radical at 139.5 GHz [57] [58]. Note that the separation between the negative and the positive enhancements is much narrower in NRF DNP compared to the SE DNP. Observation of the positive NRF DNP in the low field side, which is in opposite of SE DNP, can be explained by its dependence on the phase of the RF field.

(b) The loss in the electron polarization as a function of ω_{rf} in DSSE. The center peak is attributed to the ENDOR effect, whereas the two satellite peaks are attributed to DSSE. The experiment was performed on polystyrene doped with perdeuterated d_{21}-BDPA [59] in which the hyperfine coupling is negligible. The disposition of the satellite peak is proportional to the microwave field strength.
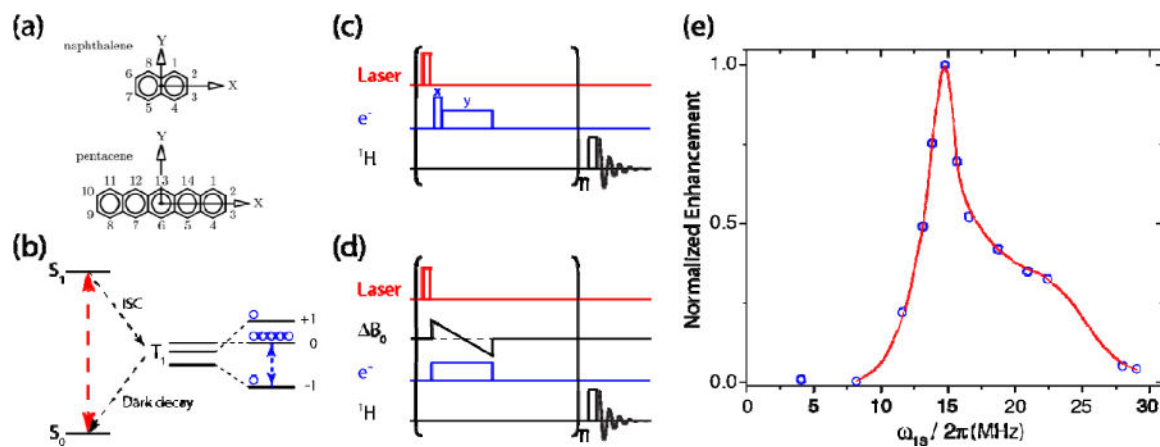
Figure 6.
(a) Naphthalene doped with pentacene, a favorite sample for NOVEL and ISE pulsed DNP.
(b) Photoexcited triplet state of pentacene created by a laser pulse. State with $S_z = 0$ is
preferably populated due to the selection rules for the intersystem crossing (ISC) process.
(c), (d) NOVEL and ISE pulse sequences on samples doped with pentacene. (e) NOVEL
matching condition shows a sharp peak and a long tail at high microwave power indicative
of higher order processes involving one electron and multiple nuclei [61].
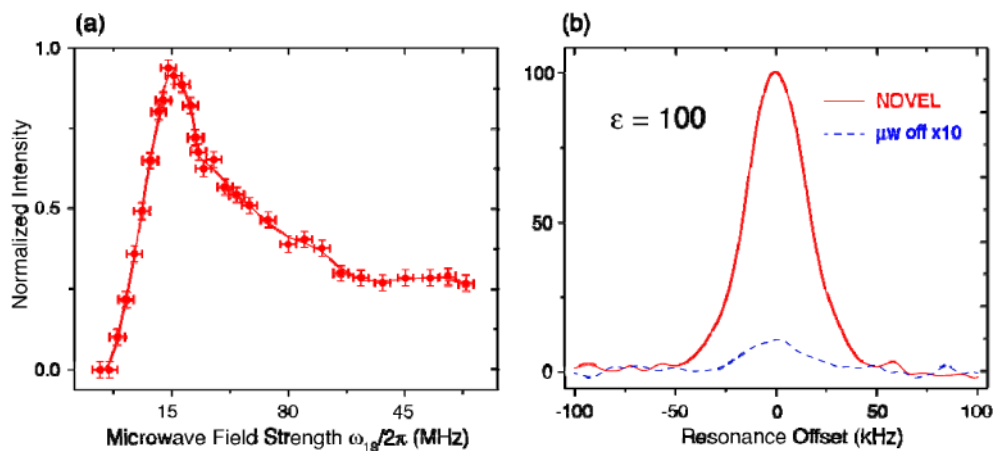
Figure 7.
NOVEL experiment at 0.35 T and 300 K on a sample of protonated polystyrene doped with 2% BDPA (mass ratio). (a) The matching condition shows a maximum at $\omega_{1S} = \omega_{0l} \approx$ 15MHz followed by a long tail at high field strength, similar to the published data in Fig. 6e. (b) Proton NMR spectra of the sample obtained with (red, solid line) and without (blue, dashed line) pulsed DNP. The spectra were acquired using solid echo sequence. A maximum enhancement of 100 was observed.
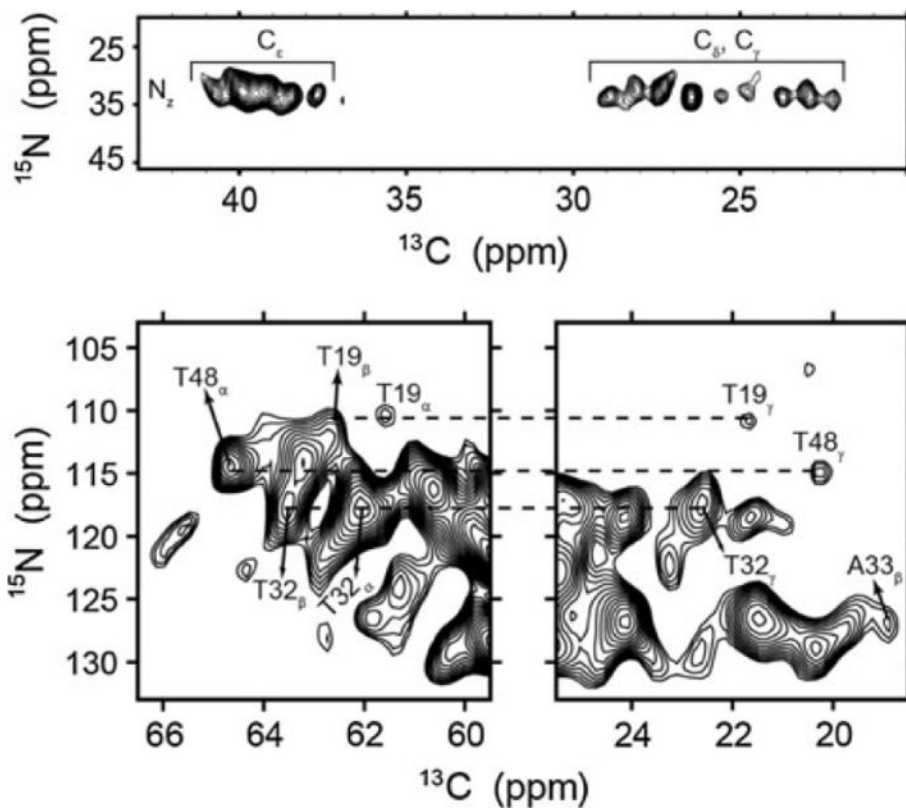
Figure 8.
Resolved regions of a ^{15}N –^{13}C correlation spectrum (NCACX) of uniformly labeled IF1 bound to E30S from Gelis, et al. [77]. Two cross-polarization transfers from ^{1}H to ^{15}N and from ^{15}N to ^{13}C preceded, ^{13}C–^{13}C exchange via PDSD (τ_{mix} = 15 ms). The top panel shows spectra from the Lys sidechains and the resolution of Ce, C and Cg ^{15}N cross peaks. This sequence permitted observation of two-bond (N-CB) and three-bond (N-CG) intra-residue correlations (lower panel) and identification of the spin systems and their assignment. The highlighted connectivities of Thr residues and the methyl group of Ala33 can be readily distinguished.
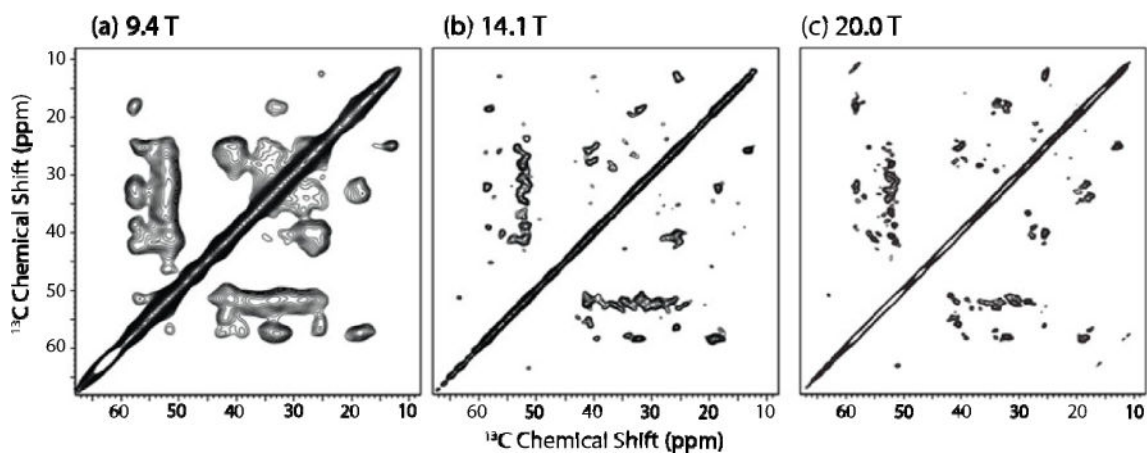
Figure 9.
Low temperature (100 K) ^{13}C-^{13}C PDSD spectra of Aβ 1–40 at (a) 9.4 T, (b) 14.1 T and (c) 20.0 T [82]. The spectra clearly show the advantage of high field which results in a progressively narrow linewidth. At 20.0 T, the spectrum at low temperature shows no compromise in linewidth compared to the one at room temperature. The linewidths of the well-resolved crosspeaks are ~ 0.7 ppm at 20 T. For example, the resolved Ser C$_\beta$ line is 160 Hz at 100 K. At 273 K it is 130 Hz.
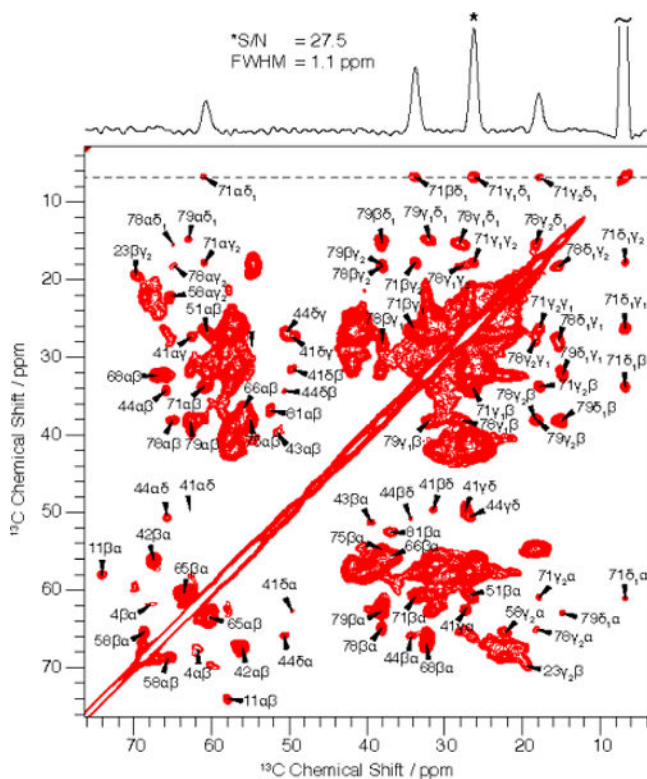
Figure 10.
^{13}C-^{13}C PDSD spectrum of protein MixH needles at 14.1 T and 100 K [76]. Excellent linewidth of ~ 1 ppm was obtained (along the dotted trace) due to the highly ordered structure of the protein assembly. The top trace illustrates the linewidths I71 cross peaks. The one denoted with an asterisk is 1.1 ppm full width and the others are of similar width.